European Journal of Wood and Wood Products
https://doi.org/10.1007/s00107-024-02132-9

ORIGINAL ARTICLE

Image-based mesh generation for constructing a virtual representation of engineered wood product samples

Patrick Grant[1] · Steven Psaltis[2] · Maryam Shirmohammadi[3] · Ian Turner[1]

Received: 13 October 2023 / Accepted: 5 August 2024

Abstract

The complex structure of timber has traditionally been difficult to model as it is a highly heterogeneous material. The density and material properties for structural species such as *Pinus radiata* (radiata pine) can vary greatly across the growth rings. Numerical simulation methods are becoming more prevalent as a method of predicting moisture migration, stress and strain distributions, and fungal/rot intrusion in engineered wood products (EWPs). All these applications require a computational mesh that captures the growth ring structure to facilitate an accurate assessment of the performance of EWPs. In this work, a low-cost image-based algorithm is developed for generating a virtual representation of a small cross laminated timber panel sample. Specifically, the proposed method results in a virtual description of an EWP sample comprised of a triangular prismatic mesh where the nodes are aligned on the growth rings of each individual timber component of the EWP, with specific wood material properties allocated to each mesh element. Each small component is treated individually and we assume there is no longitudinal variation in the density, pith location, and pith angle within the mesh structure. The initial step involves analysing an image of the end grain pattern of a single clear wood sample to identify the growth rings using a spectral clustering algorithm. Next, the centre of the tree (pith) is located through an iterative constrained least-squares algorithm to determine the pith angle. Image analysis of an anatomical image combined with the pith location allows for a constant density value to be assigned to each mesh element. The capability of this framework is then demonstrated by simulating the moisture migration and heat transfer throughout a CLT sample under atmospheric and saturating boundary conditions. Furthermore, the virtual representation provides the basis for simulating additional physical and biological phenomena, such as moisture-induced swelling, decay and fungal growth.

1 Introduction

Timber as a construction material provides many benefits over alternatives such as steel, concrete, or clay bricks; it is often cheaper, more sustainable and has comparative strength characteristics (Thomas and Ding 2018; Abed et al. 2022). This resource is readily available in Australia due to large commercial plantations spread across the country that were estimated to span 1.93 million hectares in 2019 (Downham and Gavran 2019). Timber can be sawn, peeled and glued into a variety of shapes and sizes. Sawn timber boards are restricted to the size of the tree they are cut from, while engineered wood products (EWPs) made from laminated timbers, which are constructed by gluing boards or peeled surfaces together into a panel, board, or beam, can be fabricated into much greater sizes. Throughout this paper, we will refer to each small timber board section as an individual component of the EWP sample. Timber production technologies have improved significantly over the past decade and these advancements have led to the construction of multi-storey buildings using EWPs. There are many types of engineered wood products that are used in construction, with some of the most popular being glued laminated timber (glulam) and cross-laminated timber (CLT), see Fig. 1a, b, respectively. The tallest building in Australia constructed entirely of engineered wood products, 25 King Street in Fortitude Valley, Brisbane, Queensland, stands 51 meters high and spans 10 floors. The building features a primary support

✉ Patrick Grant
p21.grant@qut.edu.au

[1] School of Mathematical Sciences, Queensland University of Technology, Brisbane, QLD, Australia

[2] School of Mechanical, Medical and Process Engineering, Queensland University of Technology, Brisbane, QLD, Australia

[3] Forest Product Innovation, Queensland Department of Agriculture and Fisheries, Salisbury, QLD, Australia

Published online: 05 September 2024

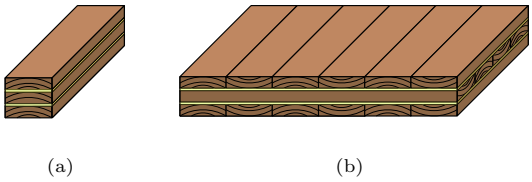

Fig. 1 Illustrative diagram of two engineered wood products. **a** Glulam beam. **b** Cross laminated timber panel (CLT). The yellow regions between the boards indicate the glue lines

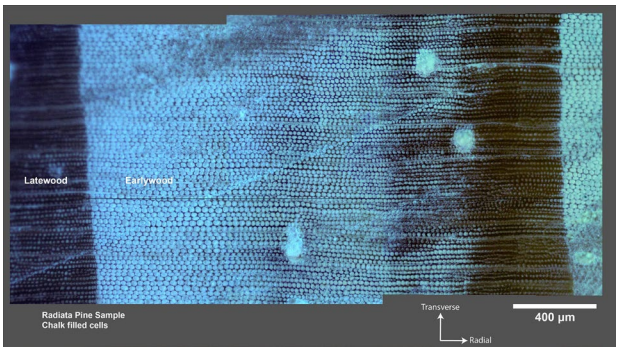

Fig. 2 Anatomical image of a radiata pine cross-section depicting a single growth ring, captured using an optical microscope equipped with a polarizing filter. The image highlights a distinct transition in cell wall thickness observed between the earlywood and latewood regions within the growth rings. Chalk was used to fill any voids within the cells. Image obtained at Queensland Department of Agriculture and Fisheries (QDAF)

structure made of glulam beams, while its walls and floors are assembled from CLT panels (Wood Solutions 2022).

Timber is a highly heterogeneous material with sharp density changes over the growth rings, making it challenging to model physical processes such as moisture migration, stresses and strains, and heat transfer throughout the product. The sharp change in density is attributed to the cellular structure of timber, as depicted in Fig. 2. Here the transition from latewood to earlywood is distinct, where the cells drastically increase in size and the cell wall thickness becomes much thinner. This abrupt change in the underlying structure of wood results in the material properties such as, thermal conductivity, bound water diffusivity, relative and absolute permeabilities, etc, varying greatly over the growth rings (Perré and Turner 2001a, b). The accurate simulation of transport phenomena is important to understand how moisture migration affects the stress and strain characteristics of the complex layered EWPs. These numerical simulation methods require the development of a virtual description of the timber being studied, which captures the rapid variation in density evident across the growth rings. A study investigating water ingress in Sitka spruce (*Picea sitchensis*) using 3D X-ray computed tomography (Burridge et al. 2021) showed a complex flow pattern, where the water quickly permeates longitudinally in the latewood section followed by the saturation of the earlywood sections. This type of flow cannot be replicated in simulations by treating the timber as a homogenous material, and this provides the motivation for developing a detailed heterogeneous virtual representation of the timber sample.

As for all organisms, timber is constructed from cells, the vast majority of which are called tracheid cells (Siau 1984). Tracheids are long and thin cells with a void space in the centre called the lumen, where water and air can flow. Pits are gaps in the cell wall that allow water and nutrients to travel between cells. Figure 2 depicts how the tracheids are tightly packed in the radial and transverse directions in a section of radiata pine. It should be noted in this figure that the longitudinal direction aligns parallel to the centre of the log. In Fig. 2, the cell diameters in the transverse direction remain roughly equal between the earlywood and latewood regions, while the cell diameter in the radial direction increases drastically in the earlywood. The growth ring width can vary anywhere between 2 mm through to 20 mm, generally decreasing further away from the pith (Ivković et al. 2013). Three anatomical images are used in assigning the density to each mesh element, which is discussed in detail in Sect. 2.7

X-Ray computed tomography (CT) scanning is often used in modelling timber as it naturally provides a three-dimensional representation of the material. CT scanning is the gold standard for timber imaging as it can provide local density, moisture content, and fibre angle information (Burridge et al. 2021; Huber et al. 2022). However, it is not always feasible to obtain a CT scan due to maximum size restrictions, cost, time, or practicality issues. Thus, in this work we have investigated the suitability of a method based on using visible light camera images to generate the mesh structure and a microscope image of the cellular structure to assign a density to each mesh element. This technology is readily available and offers an alternative to CT scanning for smaller research laboratories when more sophisticated imaging capability is not accessible.

As mentioned above, the computational modelling of heat and mass transfer in a timber board requires the use of a mesh, which is a collection of nodes connected together to form elements. These mesh elements can be comprised of any polygon in two-dimensions or polyhedra in three-dimensions. We will consider an unstructured two-dimensional triangular mesh that is then extruded longitudinally into a triangular prismatic mesh. The mesh must be carefully constructed to capture the sharp density variation present across the growth rings within the geometry. To ensure this, it is important that no element lies across the earlywood-latewood boundary as each element will have a unique density associated with it. An example of such a mesh is depicted

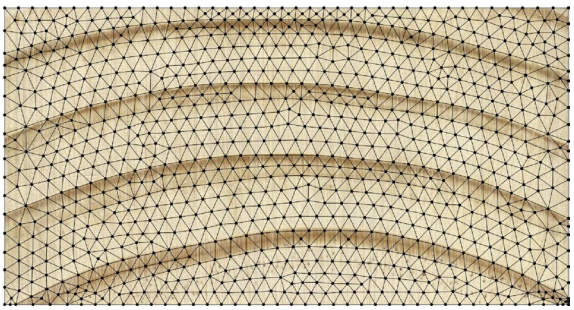

Fig. 3 Example two-dimensional triangular mesh where the nodes (dots) are connected to form triangular elements (lines)

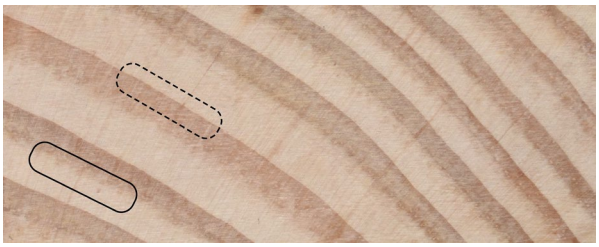

Fig. 4 End grain of a 90 mm by 35 mm board of radiata pine. The solid black box shows a region where the earlywood-latewood interface is ambiguous while the dashed region shows a distinct boundary between the earlywood and latewood sections

in Fig. 3 with the full details of its construction described in the methodology section.

There exist several methodologies for image based mesh generation, however each method is specialised for a given application. Specifically, in the medical industry where three-dimensional data is readily available from computed tomography (CT) and magnetic resonance imaging (MRI) scanning technologies, Neittaanmäki et al. (2004) develop a mesh of a human skull. Fang and Boas (2009) generate meshes for a blood vessel network, human brain, and breast tissue from three-dimensional MRI data. Kong et al. (2021) develop a mesh of a human heart using CT scan data. As mentioned previously, Burridge et al. (2021) used 3D X-ray CT scanners to determine the density of the softwood, Sitka spruce (*Picea sitchensis*), and the timber saturation under moisture ingress.

Perré (2005) developed the MeshPore software which allowed the generation of unstructured triangular meshes that align with high contrast features of the input image, either manually or automatically. However, it is worth noting that the software was developed around two decades ago, and its availability may be limited in the present context. Moreover, this software relied on high contrast images as inputs, which might not always be readily accessible. The MeshPore application was instrumental in the development of the two-dimensional version of a heterogeneous wood drying model (Carr et al. 2011, 2013; Perré and Turner 1999). Our work starts with a typical end grain image of radiata pine as exhibited in Fig. 4 obtained from a DSLR camera. This image shows two zones, one with a distinct earlywood-latewood interface and a region where the interface is more ambiguous.

The image-based mesh generation problem can be thought of as two smaller problems, involving growth ring identification and mesh generation. The growth rings can be identified using image analysis techniques and data segmentation algorithms and the mesh can be generated using available software such as Gmsh (Geuzaine and Remacle 2009). With such an open ended problem there are likely to be many possible and equally valid solution methodologies. There are many image analysis methods which can be used to identify image features including: thresholding (Liu et al. 2015), gradient watershed (Gauch 1999), edge detection (Shrivakshan and Chandrasekar 2012), and colour feature detection (Gevers et al. 2006). These techniques return data which will then need to be segmented. Similarly, there are many algorithms for segmenting the data such as: K-Means clustering (Dehariya et al. 2010), DBSCAN (Müller and Guido 2016), spectral segmentation (Meilă and Shi 2001), computer vision and machine learning (Liu et al. 2012).

The main aim of this work is to develop a low cost, accessible, method for generating a complete virtual description of a small engineered wood product sample. To achieve this, we start by generating a mesh of an individual timber component using a cross-sectional image captured by readily available camera technology. Mathematical tools available in MATLAB (The Mathworks, Inc. 2022a) are used to identify the timber material property information, such as density variation and pith angle, that is subsequently accommodated in the mesh structure generated using the Gmsh software (Geuzaine and Remacle 2009). These individual components are then assembled into the required EWP sample. Our water ingress case study demonstrates the ability of the virtual representation to support the modelling of complex moisture migration flows. However, in this work we are not quantitatively analysing any model parameters or data of the resulting flow patterns. We aim to extend this work to accurately simulate heat and mass transfer and swelling of EWP samples in the future. A key feature of this future research will be the calibration of model parameters using experimental data.

There are several assumptions and simplifications that we have made that streamline our approach. Firstly, because we are working with small wood sample sizes (with a maximum longitudinal dimension of approximately 10 cm), we assumed the variation in the longitudinal direction in the growth ring structure, pith location, and pith angle is

negligible. We have also assumed that we are modelling clear wood samples that do not contain knots. Furthermore, the EWPs under consideration are constructed of radiata pine sapwood samples.

The paper is organised as follows. In Sect. 2, we outline the methodology used to develop the virtual three-dimensional model of the EWP samples. This discussion includes the chosen timber imaging techniques, image masking method, generation of the radial-transverse cross-sectional mesh and extrusion in the longitudinal direction for each component of the EWP. It also covers the algorithm developed for locating the pith, estimation of the pith angle, and the allocation of wood density to mesh elements, which are all used in the evaluation of the material properties required for the heat and mass transfer model (TransPore) that include permeability, capillary pressure, bound water diffusivity, and thermal conductivity. In Sect. 3, the individual components are combined to create the virtual representation of the EWP sample. We also present visualisations of the evolution of the moisture, temperature, and saturation fields over a 64 h period for an application involving a two-component CLT panel sample. The EWP is subjected to water ingress on one of the RT faces of the top component, with imperfect contact boundary conditions imposed for nodes that lie on the glue line. Additionally, with a set of psychrometric conditions on all other faces that is representative of typical environmental conditions experienced in Brisbane, Australia. In Sect. 4, we discuss the outcomes of the study and then provide the conclusions of the work in Sect. 5.

2 Methodology

The example used in this paper to demonstrate our methodology is a three layer cross-laminated timber (CLT) sample where each individual small board component has the dimensions of $0.09\,\text{m} \times 0.045\,\text{m} \times 0.09\,\text{m}$ in length, width and depth (longitudinal) respectively. The proposed methodology for generating the mesh of an individual timber component can be summarized as follows. A photograph or a scan of the end grain pattern of a clear wood sample serves as the starting point for generating the mesh. Initially, an unstructured two-dimensional triangular mesh (in a radial-transverse cross-section) is generated using the end grain image. Next, the pith is located using an iterative constrained nonlinear least squares algorithm fitting multiple circles through the identified growth rings, which allows for the computation of the pith angle. The density of each triangular mesh element is then computed by first defining the intra-growth ring fractional radial position (FRP), which is a proportional measure of the distance a given mesh element is through the growth ring. The density across the growth ring is computed by analysing an anatomical image of the cellular structure, where a five-point logistic (5PL) function fit is constructed to map the FRP to a density value. The triangular mesh is then extruded into the longitudinal direction using triangular prismatic mesh elements. The meshes of multiple timber components are combined to create a mesh for the entire EWP sample. Finally, moisture, temperature, and density based material properties can now be computed for each mesh element, resulting in the full virtual representation of an EWP sample. The majority of the code is written in MATLAB, and Gmsh is used to mesh the geometry specified by the MATLAB codes. All code and supporting files are uploaded to GitHub.

2.1 Timber imaging

The process of mesh generation commences with the capture of an image of the end grain of a clear wood sample. As mentioned in the introduction, one of the requirements of our modelling strategy is to use readily available, inexpensive equipment and we have found that either a digital single lens reflex (DSLR) camera or a flatbed scanner were suitable for this task. For this research we captured the images using an Epson V600 flatbed scanner (in 800 dots per inch mode) and a Nikon D500 21 megapixel DSLR camera. While testing we found it was best to capture these images in the highest resolution possible as they can be downsampled later. Perspective distortion (also called wide-angle distortion) can cause the resulting image of the timber to be warped. This effect occurs when using a wide-angle lens which is positioned close to the wood sample. This can cause objects closer to the edge of the frame to appear warped which can make the end grain pattern non-rectangular, thus leading to a poor virtual reconstruction. This effect is conceptualised in Fig. 5, whereby perspective warping can be mitigated by using a lens with a longer focal length and positioning the lens further away from the sample. Positioning the camera more than 1.5 m away with a focal length greater than 100 mm full frame equivalent minimised this effect for our imaging needs. A flatbed scanner is able to obtain higher resolution images and does not have the perspective warping issue as the scan head moves in parallel with the sample. However, the size of the EWP sample is limited by the size of the scanning bed.

2.2 Image masking

Once a clear, in focus image is obtained it is converted to grayscale and the size of the image is reduced so that the long side has approximately 250 pixels (the short side ranges from approximately 100–150 pixels), which we found has produced acceptable results and speeds up processing time. Next, a Gaussian blur (with standard deviation of $\sigma = 0.5$, chosen through testing) is applied to the image to reduce

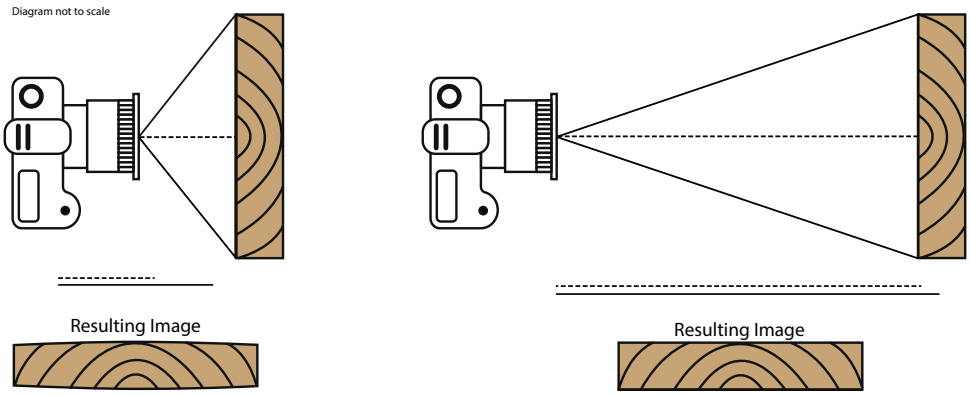

Fig. 5 Schematic representation of perspective warping. The difference in distance between the edges (solid line) and the centre (dashed line) of the wood sample is much greater when the camera is close to the sample. An image taken using a setup similar to that on the left could result in the edges of the board sample becoming warped (as seen in the resulting image), while the right setup would result in the expected rectangular image of the sample

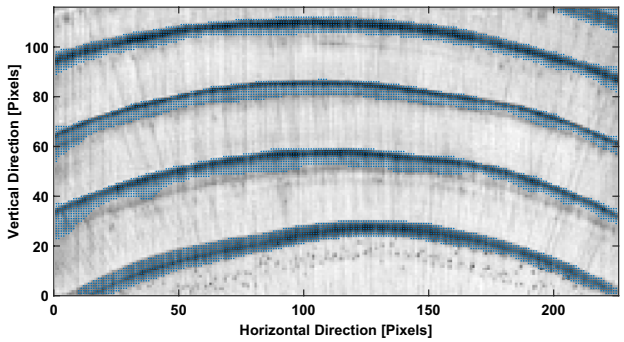

Fig. 6 Example image mask of a reduced size image where the blue dots highlight the flagged pixels in the image mask

high fidelity noise. Then, a mask is generated which is a logical array having the same size as the image. The mask contains either zeros or ones, a one indicates pixels in the darker latewood sections and a zero indicates pixels in the earlywood, refer Fig. 6. The MATLAB function `graythresh` (The Mathworks, Inc. 2022a) is used to obtain a thresholding value, where pixels darker than the threshold are marked. Lastly a median filter is applied to remove small isolated regions of masked pixels that do not correspond to the latewood region (again refer Fig. 6).

2.3 Spectral segmentation

Once the image mask has been generated and filtered, the pixels in the mask can be converted into a list of data points containing the horizontal and vertical position. The data can now be segmented using a recursive bipartitioning spectral clustering algorithm. This algorithm is desirable as it is a high performance data segmenting algorithm where orientation does not matter (Cour et al. 2005). The process begins with the generation of a similarity matrix $\mathbf{W} \in \mathbb{R}^{n\times n}$ where n is the number of pixels to be segmented (Von Luxburg 2007). The entries in the similarity matrix can be constructed to take into consideration different data property features, some examples include: spatial distance, pixel colour, pixel light intensity (Jia et al. 2014). For our implementation we have used spatial distance between the points in the image mask. The graph Laplacian, $\mathbf{L} \in \mathbb{R}^{n\times n}$, is then generated as:

$$\mathbf{L} = \mathbf{D} - \mathbf{W}, \tag{1}$$

where $\mathbf{D} \in \mathbb{R}^{n\times n}$ is the diagonal matrix,

$$\mathbf{D}_{ii} = \sum_{j=1}^{n} \mathbf{W}_{ij}, \quad i = 1, \ldots, n. \tag{2}$$

The elements of $\mathbf{W}$ are computed as a Gaussian weighted spatial distance between each point pair in the data set,

$$\mathbf{W}_{ij} = \exp\left[-\frac{\|\mathbf{x}_i - \mathbf{x}_j\|_2^2}{2\sigma^2}\right], \tag{3}$$

where $\mathbf{x}_i$ and $\mathbf{x}_j$ are the ith and jth position vectors in the image mask respectively and σ is a parameter which controls the size of the point neighbourhoods. The method for selecting σ is discussed towards the end of this subsection. The eigenvalues and eigenvectors of the graph Laplacian, $\mathbf{L}$, are computed and sorted in ascending order. The signs of the elements in the eigenvector that corresponds to the second smallest eigenvalue (Fiedler vector) designate which bipartition that point is in, see Fig. 7a. The second vector is chosen as the elements in the first eigenvector are all constant with a value of $1/\sqrt{n}$. This process is repeated until all data sets are segmented. The outcome is exhibited in Fig. 7b.

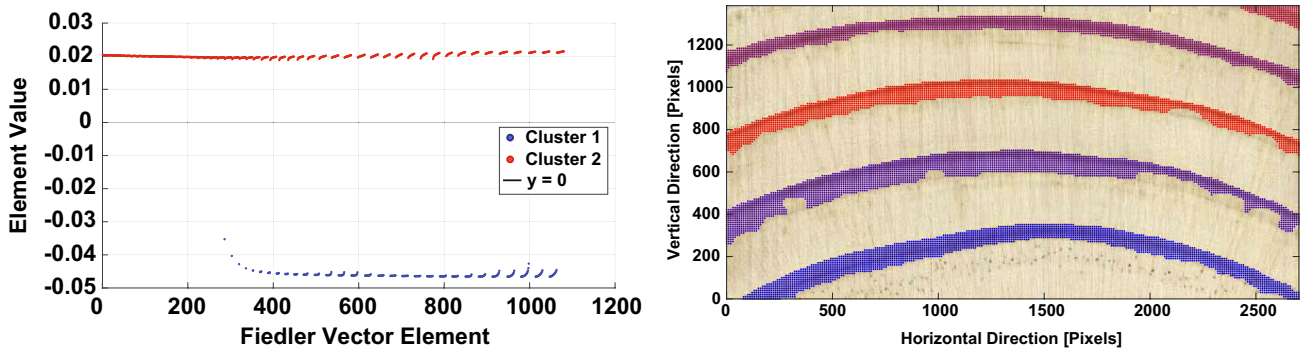

(a) (b)

Fig. 7 **a** Example Fiedler vector values, each element of the vector corresponds to a point in the image mask where the sign of the value determines which cluster that point lies in. **b** Final result of clustering where each segment is a different colour

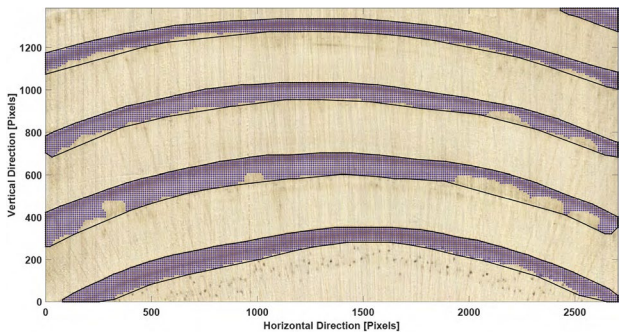

Fig. 8 Boundaries determined using MATLAB's `boundary` function, with shrink factor $S = 0.15$

Notice that there are partially incomplete regions evident in the image mask, on the bottom side of the two central growth rings in Fig. 7b. These regions form as a result of the latewood section not being as dark in these sections and thus, were not captured in the thresholding stage. These incomplete regions can be filled by fitting a boundary around the points in each newly segmented growth ring as illustrated in Fig. 8. The boundaries are computed using the inbuilt MATLAB function: `boundary` (Mathworks, Inc. 2022), which takes the x and y positions of each point and a shrink factor parameter $0 \leq S \leq 1$ as inputs. MATLAB's `boundary` function generates an alpha shape which returns a triangulation that encloses a set of data points when given a radius, α (Edelsbrunner and Mücke 1994). The α radius is directly correlated to the shrink factor, S, in the `boundary` function. When $S = 0$ the boundary is the convex hull of the data points, and $S = 1$ generates the tightest single region boundary around the points. As the shrink factor decreases from one to zero the boundary becomes less compact. The boundaries depicted in Fig. 8 use a shrink factor of $S = 0.15$. During testing it was found that this choice of shrink parameter is ideal as it follows the edges of the growth rings closely and bridges the gaps evident in the incomplete regions identified in Fig. 7b. Larger values of S result in the boundary not filling these regions and smaller values start filling in too much as the boundary approaches the convex hull. The area enclosed by these boundaries is then filled with data points and these new regions are used when fitting the smoothing splines for the earlywood–latewood boundaries that will be outlined in Sect. 2.4.

To determine if a bipartition (cut) is optimal, we check if the boundary elements of each data set lie directly adjacent to each other. This way we ensure that each segment contains only one growth ring. The left side of Fig. 9 presents an example of a suboptimal bipartition. In panels A and B, observe that the boundary points of the two clusters (black circles) are next to each other. An optimal cut is achieved by reducing the σ parameter thus obtaining a different cut as depicted in panels C and D. The right side of Fig. 9 presents an optimal cut.

The coding implementation uses the MATLAB function `spectralcluster` as it can automatically determine the σ parameter. The function uses a median distance to the nearest neighbour heuristic for determining the value of σ (Mathworks, Inc. 2022). The function also takes the number of clusters as an input, we set it for 2 clusters as we don't know the number of growth rings at the start of the process and so we can still apply our bipartitioning algorithm. The automatically determined heuristic can be computed and if a suboptimal bipartition is obtained another σ value is sampled uniformly from the interval between 1 and two times the neighbour heuristic until an optimal bipartition is made. This process has always resulted in successful segmentation on all the image masks tested thus far. We also found that the DBSCAN (MATLAB inbuilt function) algorithm was able to successfully segment each of the masked growth rings when given the correct input parameters: epsilon neighbourhood and minimum number of core points (Müller and Guido 2016).

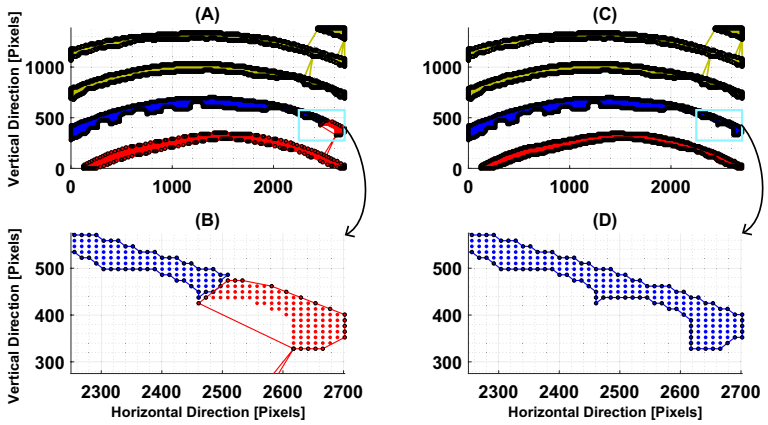

Fig. 9 Example bipartitions, where the yellow regions represent already-segmented growth rings, and the red and blue regions indicate the bipartitions currently under consideration. Panels A and B illustrate suboptimal cuts, which involve cutting through a growth ring. Panels C and D show optimal cuts with reduced σ, which involve segmenting the entire growth ring

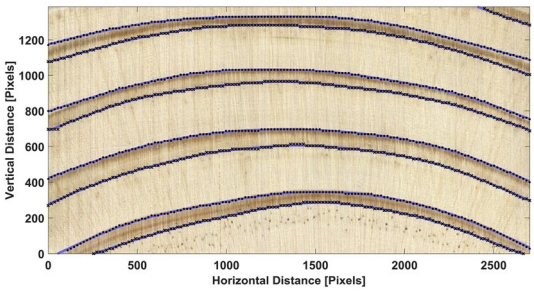

Fig. 10 Fitted cubic smoothing splines through the earlywood-latewood boundaries

However, the spectral clustering function allows us to implement a check for suboptimal bipartitions by only updating one parameter instead of the two needed for DBSCAN.

2.4 Determining the Earlywood–Latewood boundaries

The points on the boundary of each growth ring section are found using the previously mentioned `boundary` function with $S = 1$, to ensure the tightest single region boundary is identified. The boundary points above and below the latewood sections are then isolated and a cubic smoothing spline is fitted through the boundaries. The result of this process is shown in Fig. 10.

The piecewise cubic smoothing spline $f(x)$, over the interval $x \in [a, b]$, with smoothing parameter $p \in [0, 1]$ minimizes the following functional (De Boor 1978):

$$\underbrace{p \sum_{i=1}^{n} |y_i - f(x_i)|^2}_{\text{Least Squares Term}} + \underbrace{(1-p) \int_a^b \left(\frac{\mathrm{d}^2 f}{\mathrm{d}x^2} \right)^2 \mathrm{d}x}_{\text{Roughness Penalty}}, \tag{4}$$

where x_i, y_i are the x- and y-coordinates of the boundary points respectively, and n is the number of points. The first term is a standard least squares minimization and the second term is a roughness penalising term. When $p = 1$ the smoothing spline simply interpolates all the data points, when $p = 0$ the minimization problem reduces to a linear least squares estimate. For intermediate values the smoothing spline lies somewhere between the piecewise smooth cubic interpolation and the linear least squares estimate (De Boor 1978). Reinsch (1967) recommends a value of $p = 1/(1 + h^3/6)$, where h is the average spacing of the data. MATLAB's curve fitting toolbox is used to generate and evaluate the splines (The Mathworks, Inc. 2022b).

2.5 Generating the computational mesh

The benefit of using splines is that they are defined over the whole domain. They also smooth out the noise inherited from the image masking process in the input data, providing a more realistic fit to the growth ring boundaries. Next, we need to generate the mesh (using Gmsh) from the fitted smoothing splines. Gmsh is an open source meshing software package that provides the user with many powerful tools for mesh generation (Geuzaine and Remacle 2009). The user defines the geometry of the object to be meshed alongside the desired level of refinement, then Gmsh will generate the mesh for that geometry and refinement. The meshes can be one-, two- or three-dimensional and consist of many element types, for example: triangular, quadrilateral, tetrahedra, triangular prism, etc. The strategy we adopt is to generate a two-dimensional unstructured triangular mesh that describes the growth ring variation in the RT cross-section, then extrude the mesh (in the longitudinal direction) to produce a three-dimensional triangular prismatic mesh for each component of the EWP sample.

When passing this mesh to the TransPore model to simulate heat and mass transfer processes in wood, see for

example Perré and Turner (2002); Carr et al. (2011), it is important that there only exists one material type density allocated to each triangular element, either the earlywood or latewood. By placing the nodes of the mesh on the growth ring boundaries it ensures that the triangular elements will not cross this boundary. For the mesh generation, we are only interested in the latewood to earlywood (from the pith, discussed in Sect. 2.6) spline because that is where the sharp density variation arises. We have used both splines when locating the pith to improve accuracy, refer to Sect. 2.6 for more details. Control over the mesh refinement is also required, especially on the edges of the sample and along the internal growth ring boundaries, as these are the locations where steep gradients may arise in the moisture content fields. Mesh refinement is controlled by specifying the number of nodes along these splines, which is achieved by defining the splines as a Transfinite curve type in Gmsh. The process of mesh generation commences with the construction of smaller rectangular boxes where the mesh refinement will be specified within that box. Figure 11 demonstrates how each part of the splines passes through each box. Careful consideration has been given to where the curves briefly enter a zone and leave quickly. For these scenarios, the refinement of the previous box is applied, refer to the top right corners of the two internal boxes in Fig. 11.

The splines that pass through different refinement zones get split into multiple smaller sub-splines, one for each zone. Gmsh handles mesh refinement in several ways however it was found that defining the number of nodes desired along each sub-spline produced suitable meshes. The length of each segment is computed and the corresponding node count applied. For example, if a sub-spline is 283 pixels long and is located in the 25 pixels per node (PPN) section then there would be 11 nodes placed along that segment (including the two end nodes). Figure 12 displays a mesh that is refined more towards the edges of the domain, showing that a higher PPN results in a coarser mesh.

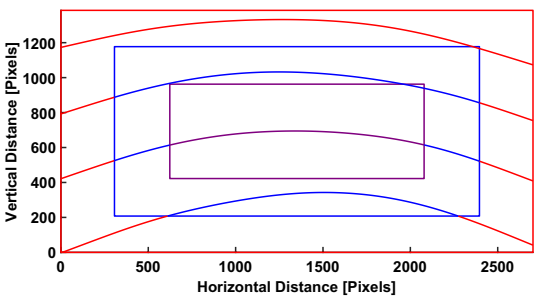

Fig. 11 Example geometry refinement zones with two internal boxes. It can be observed that the splines that only slightly extend into the top right corner of the internal boxes do not undergo any refinement changes

Using the `extrude` function within Gmsh the two-dimensional mesh can easily be extended into the longitudinal dimension. Figure 13 depicts the full three-dimensional mesh generated from the RT cross-sectional mesh shown in Fig. 12, extruded with 21 layers (including the initial two-dimensional mesh). To specify ℓ layers of triangular prisms the number of layers option for the extrude function needs to be set to $\ell + 1$ in the Gmsh geometry file. Mesh refinement factors are carefully considered with the view of minimising the total number of mesh elements used for the virtual representation of each component of the EWP, so that overall computation times for numerical simulations can be minimised. The mesh data consists of the nodal positions in three-dimensional space, element connectivity information, surface quadrilaterals and triangular faces among other subsidiary mesh information. Gmsh can export the mesh data in many widely used formats, for our implementation we export the mesh data as a MATLAB script file.

2.6 Pith location algorithm and pith angle computation

Material properties important for modelling moisture migration and heat transfer (such as effective thermal conductivity, bound water diffusivity, etc.) are defined in the

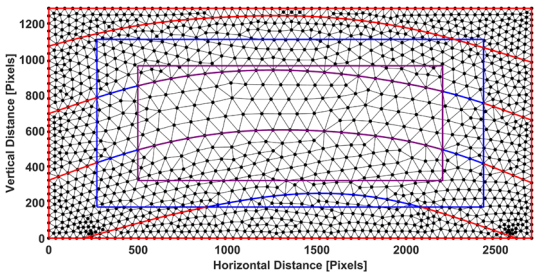

Fig. 12 Example mesh with three refinement zones, starting with 45 pixels per node (PPN) in the red zone, 60 PPN in the blue zone and 90 PPN in the purple zone

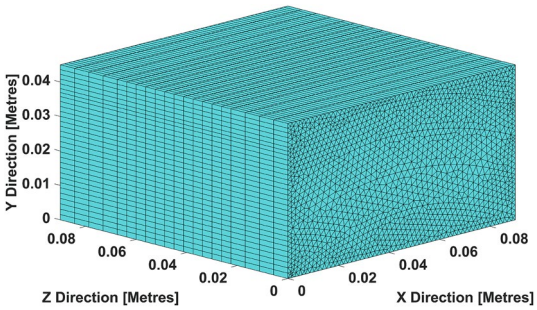

Fig. 13 Example three-dimensional triangular prism mesh with 21 non-uniformly distributed layers

radial, transverse and longitudinal directions of the timber board (Perré and Turner 2001a, b). For numerical simulation these material properties need to be defined in the x, y and z directions. Thus, the pith location and pith angle needs to be estimated and computed respectively. A standard transformation matrix must be applied to the material properties defined in the RTL framework to map them to the x, y and z coordinate directions. To illustrate, we exhibit how this rotation is applied to the effective thermal conductivity $\tilde{\mathbf{K}}_{\text{eff}}$ tensor:

$$\tilde{\mathbf{K}}_{\text{eff}} = \begin{pmatrix} K^R_{\text{eff}} & 0 & 0 \\ 0 & K^T_{\text{eff}} & 0 \\ 0 & 0 & K^L_{\text{eff}} \end{pmatrix}, \tag{5}$$

where K^R_{eff}, K^T_{eff}, and K^L_{eff} are the effective thermal conductivities in the radial, transverse and longitudinal directions respectively. The rotated effective thermal conductivity tensor is then expressed as follows:

$$\mathbf{K}_{\text{eff}} = \mathbf{R}^{\text{T}} \tilde{\mathbf{K}}_{\text{eff}} \mathbf{R}, \tag{6}$$

with the following rotation matrix $\mathbf{R}$, given by

$$\mathbf{R} = \begin{pmatrix} \cos\theta & -\sin\theta & 0 \\ \sin\theta & \cos\theta & 0 \\ 0 & 0 & 1 \end{pmatrix}, \tag{7}$$

where θ is the pith angle. This angle is defined between the horizontal axis located at the pith and the chosen sample mesh point, refer Fig. 14a. It is assumed to be unchanged throughout the longitudinal direction of the component.

To determine the pith angle for each node in the mesh, it is necessary to estimate the location of the pith. To do this, we sample points from the cubic smoothing splines previously discussed in Sect. 2.4 and fit a circle through each spline, in a least squares sense, to identify the radius and the center of the circle. Consider the equation for a circle centred at (x_0, y_0) with radius R:

$$(x - x_0)^2 + (y - y_0)^2 = R^2, \tag{8}$$

which can be expressed as:

$$x^2 + y^2 = R^2 + 2xx_0 + 2yy_0 - x_0^2 - y_0^2, \tag{9}$$

then the subsidiary coefficients can be absorbed into a new variable $A = R^2 - x_0^2 - y_0^2$, to give

$$x^2 + y^2 = A + 2xx_0 + 2yy_0. \tag{10}$$

Using Eq. (10) and the selected data points from the spline, the coefficients A, x_0 and y_0 can be found using least squares. The radius can be recovered with:

$$R = \sqrt{A + x_0^2 + y_0^2}. \tag{11}$$

The process is performed twice for each growth ring to determine the pith location and radius for the two borders of the latewood section. This yields a set of potential pith locations and radii. In the subsequent iteration, we recalculate the least squares fit, constraining the pith locations within a box with a height and width that equals half of the standard deviation of the circle centers from the previous iteration, refer to electronic supplementary material 2 (Fig. 1) for the results obtained after six iterations. Figure 15a presents the approximate pith location for a backsawn timber wood component of radiata pine after 15 iterations. This method allows for an approximate pith location to be found, which can then be used to allocate the pith angle throughout a given component. We reinforce the assumption of no longitudinal variation through these small samples so we can use the same pith angle longitudinally through the sample. With the pith location computed, the pith angle can be found for each element and node of the mesh using basic trigonometry, refer Fig. 15b. The material properties can now be defined in the x, y and z directions which is needed for numerical simulations using the TransPore model.

Recent published research has used a similar approach to locate the pith of Norway spruce timber (Habite et al. 2020), to achieve good estimations of the pith locations and average annual growth rate (growth ring width). Their method starts with an initial estimate of the pith location and average growth ring width, to which a cost function of the

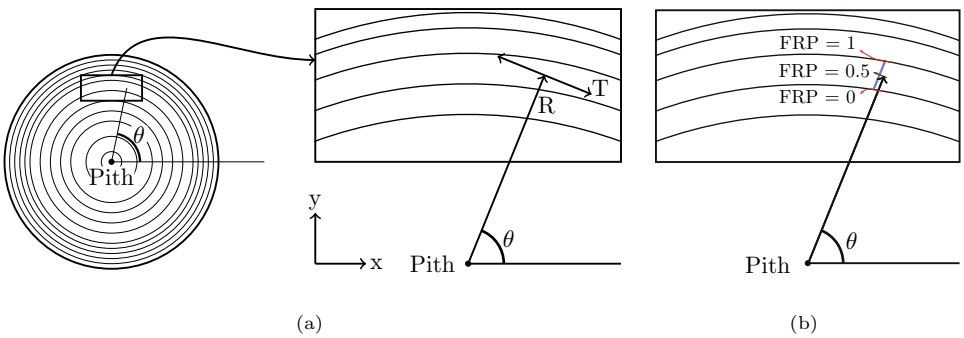

Fig. 14 **a** Description of the pith angle θ, where R and T represent the radial and transverse directions respectively. **b** Visual description of the fractional radial position (FRP) which is a relative measure of how far a point is through a given growth ring

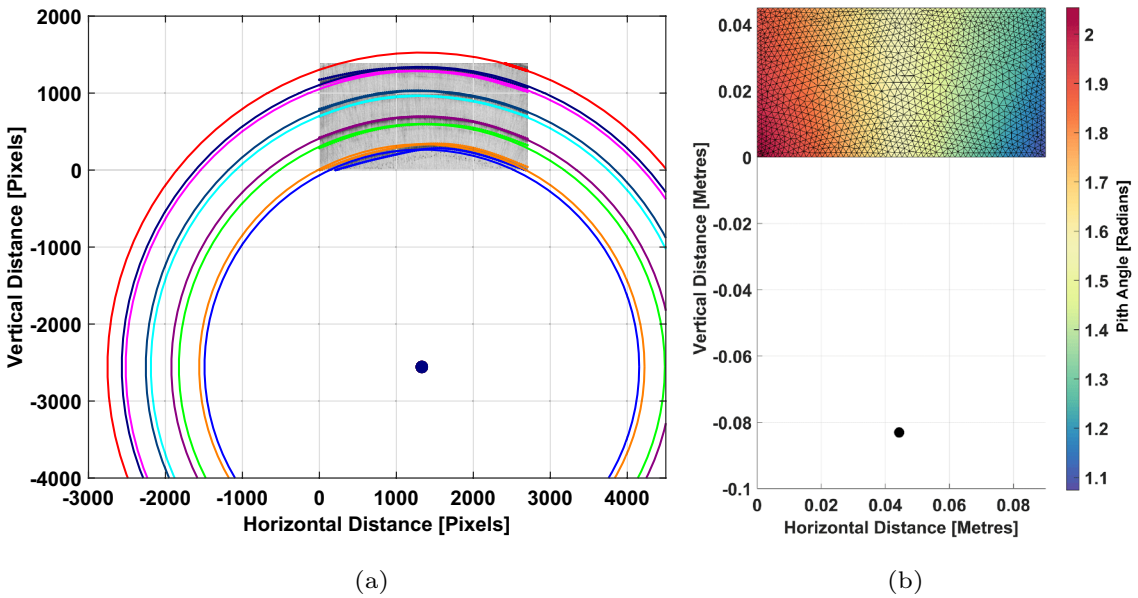

Fig. 15 **a** Fitted circles through the earlywood–latewood interface with an approximate pith location shown as the black dot, measured in pixels. **b** The pith angle (radians), θ, of the backsawn board

pith locations and ring width is determined and then minimised. They assumed that the growth ring width is constant throughout the whole board, which for Norway spruce is a valid assumption. This assumption may be breached when considering timber species with non-uniform growth ring widths and spacing, such as radiata pine. Comparisons to this algorithm are made later in the discussion section. The method presented in this article allows for varying growth ring sizes as each earlywood–latewood boundary is considered independently, instead of treating the latewood section of the growth ring as one entity. In later works, Habite et al. (2022) used a one-dimensional convolutional neural network to achieve good estimates of the pith location, where input was a horizontal slice through visible light images of the four non-end grain faces of the board.

2.7 Mesh density

Computed tomography (CT) and magnetic resonance imaging (MRI) scanners have been demonstrated to generate 3D profiles of timber density and moisture (Burridge et al. 2021; Lazarescu et al. 2010). However, the requirement for isolated timber sections, together with the need for specialized training and expensive equipment make their practical usage challenging. We propose a method for determining local density values by computing the intra-growth ring fractional radial position (FRP) across the component. We then use a five-point logistic function to map the FRP to the density. This function is chosen as the parameters convey a physical meaning which we will discuss shortly. The data for the fit is obtained by sectioning an anatomical image into strips and computing the proportion of those strips that are pixels of the cell wall, then we multiply this proportion by the known cell wall density (1530 kg m^{-3}) as demonstrated in Perré (1997), refer to Fig. 17 for a conceptualisation. Lastly, each element in the two-dimensional triangular mesh is assigned a constant density value, which is then used for all triangular prismatic elements emanating from that triangular face extruded into the longitudinal direction.

To determine local density, the first step is to identify which growth ring boundaries the centroid of each mesh element lies between. We only need to consider the latewood to earlywood boundary (from the pith) as that is where the sharp change in density exists. Next, the FRP is computed by seeing how far through a given growth ring each element centroid is located, refer Fig. 14b. The FRP is used as the relative distance between each growth ring, and scaling the distances between zero and one allows the density to be easily computed by applying the five-point logistic function that is defined over the domain [0,1]. Each spline is extended outside the sample boundaries so that the distance for points on the edge can still be computed.

For regions where there is no spline between the pith and the element, (regions labelled 0 in Fig. 16a), we use the next growth ring (regions labelled 1) splines. The idea is to use information from the neighbouring growth ring as if the element was inside that growth ring. Similarly this idea is applied to elements where there is no spline that intersects the pith-element ray after the element (regions labelled 4), however we use information from the previous growth ring

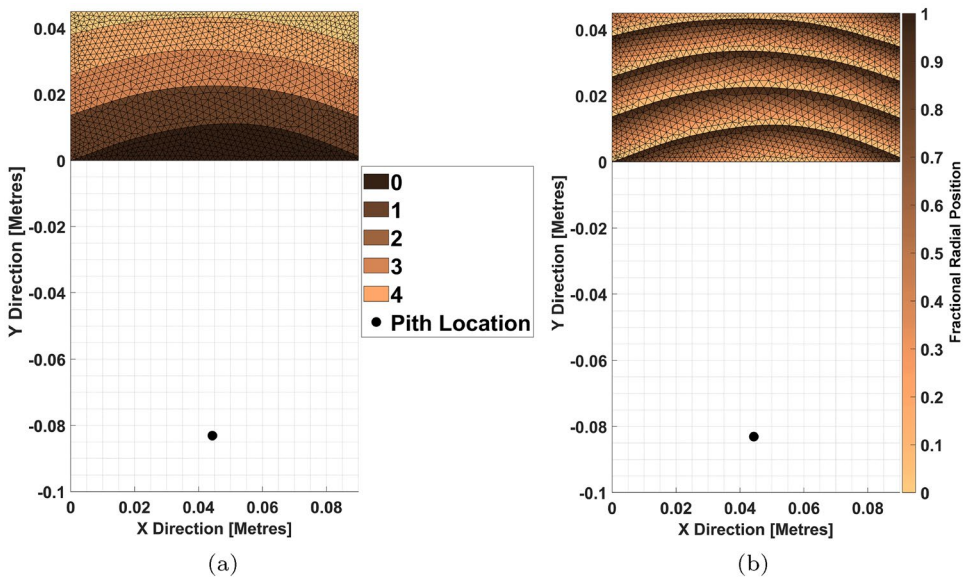

Fig. 16 **a** Regions which indicate how many growth rings a ray between the pith and each mesh element would pass through. **b** The fractional radial position across the whole wood sample

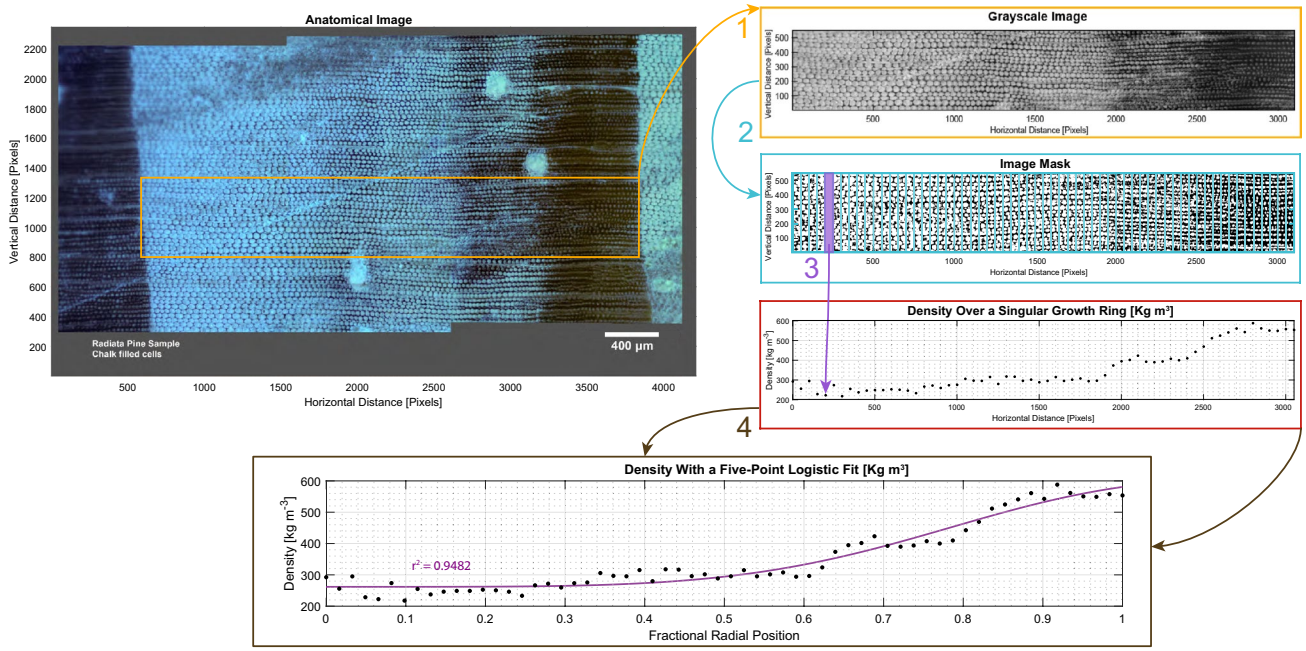

Fig. 17 The flowchart illustrates the process for determining density values within a single growth ring. The four main steps, indicated by arrows and corresponding step numbers, are: (1) selection of the desired region and conversion to grayscale, (2) application of an image mask to identify the cell wall pixels using MATLAB's `adaptthresh` function, (3) calculation of the proportion of black pixels within each column and multiplication by a solid density ρ_s, (4) normalisation of horizontal pixel distance to a fractional radial position and fitting of a five-point logistic function

(regions labelled 3) in this case. This process enables the centroid of each mesh element to have assigned a FRP along the growth ring.

Next the five-point logistic (5PL) function (Koya and Goshu 2013) is used to convert the FRP to a density value for each element. Each parameter in the 5PL function has a distinct physical characteristic that affects the shape of the curve, where the five-point logistic function is defined as:

$$\rho(x) = \beta_0 + \frac{\beta_1 - \beta_0}{\left(1 + \left(\frac{x}{\beta_2}\right)^{\beta_3}\right)^{\beta_4}}, \tag{12}$$

where ρ is the density, x is the fractional radial position, β_0 and β_1 are the maximum and minimum densities respectively, β_2 is the inflection point (when $\beta_4 = 1$), β_3 is the slope factor which describes the steepness of the curve and β_4 is an asymmetry coefficient (Psaltis et al. 2021). The 5PL is often used in many biological applications where growth is concerned (Koya and Goshu 2013) and has previously been used for fitting the modulus of elasticity in timber (Psaltis et al. 2021). We extend its application to fitting the density of radiata pine to the FRP.

The radial density is computed using image analysis on three anatomical images of timber acquired at the Queensland Department of Agriculture and Fisheries experimental facility located at Salisbury in Brisbane, using the method described in Perré (1997). The three images chosen to determine density have varying thicknesses of the latewood band. The two images exhibited in electronic supplementary material 1 (refer Figs. 1 and 2) are growth rings with relatively thin and thick latewood regions of the growth rings respectively. The anatomical image depicted in Fig. 2 has a relatively medium latewood band thickness. To extract the density across the growth rings, the images are thresholded so the cell wall pixels are masked, then divided into vertical strips and the proportion of each strip that is the cell wall can be computed. This proportion is then multiplied by the solid phase density of timber, $\rho_s = 1530$ kg m^{-3}. The horizontal distance of each image encompasses a single growth ring, the x-coordinate data is then rescaled to be between 0 and 1, which is fitted using the 5PL function. This process is conceptualised in Fig. 17 using the medium thickness anatomical image. Table 1 presents the coefficients for each image (thin, medium and thick), alongside the r^2 value, and the upper and lower bounds for each parameter. The coefficients are determined by completing a constrained least-squares fit using MATLAB's Curve fitting toolbox (The Mathworks, Inc. 2022b).

A simple heuristic based on the the percentage of latewood within each growth ring is used to determine which one of the 5PL curves to use for a given growth ring. The latewood area can be computed by using the splines either side of the growth rings, refer to Fig. 10, using MATLAB's `polyarea` function. The area of the entire growth ring can then be calculated, which allows for the percentage of the latewood that occupies a growth ring to be computed. We have designated that the thin 5PL function is used in growth rings with less than 15% latewood area, the middle curve is chosen for percentages between 15 and 25%, and the thick curve is selected for latewood percentages above 25%. These values are chosen so that all three curves are selected when developing our EWP sample and to provide further heterogeneity into the model. If an element is identified for a growth ring that is not fully present (regions labelled 0 and 4 in Fig. 16a), the median of all the selected curves for elements which have a complete growth ring is taken. Figure 18a shows an example where each mesh element is assigned a density as computed from two of the 5PL functions. This can then be extruded from the two-dimensional triangular mesh into a three-dimensional triangular prismatic mesh, as shown in Fig. 18b.

Table 1 Fitted parameter values for the five-point logistic function described in Eq. (12) for the three anatomical images used

Coefficient	Thin	Medium	Thick	Lower bound	Upper bound
β_0	800	573.3	648.6	400	800
β_1	282.1	262.8	305.2	0	400
β_2	1.2	1.1	1.3	0	10
β_3	10	5.1	2.9	0	10
β_4	10	9.4	10	0	10
r^2	0.6374	0.9482	0.8506	–	–

Refer to electronic supplementary material 1 (Fig. 3) for the plots of these three functions

2.8 Initial moisture content field

With the virtual representation now constructed, we can compute the initial moisture content field. If the average moisture content of the component, $\overline{X}$, is below fibre saturation point, X_{FSP}, then we take the initial moisture content field as constant throughout the component at the average value. Otherwise, we need to determine the spatial variation of the moisture content field. The main driver of moisture migration (when $\overline{X} > X_{\mathrm{FSP}}$) is capillary pressure. The initial moisture content field is reached when the capillary pressures across the component are in equilibrium (Perré and Turner 2002). The local capillary pressure, $P_c(S_{\mathrm{w}}^{(i)}, \rho_0^{(i)}, T)$, is defined in terms of the free water saturation, density, and the temperature and its functional form is described in Perré and Turner (2001a). This process is applied to the two-dimensional triangular mesh with the moisture content being extruded into the three-dimensional mesh. Each component of the EWP is treated individually and can have different average initial moisture contents. To compute the initial moisture content field, the averaged timber density at each node is required and we construct control volumes around each node in a vertex-centred manner, as demonstrated in Carr et al. (2011). The average density $\rho_0^{(i)}$ defined at each node i is described as follows:

$$\rho_0^{(i)} = \frac{\sum_{j=1}^{m} \rho_0^{(j)} A_j}{\sum_{j=1}^{m} A_j}, \tag{13}$$

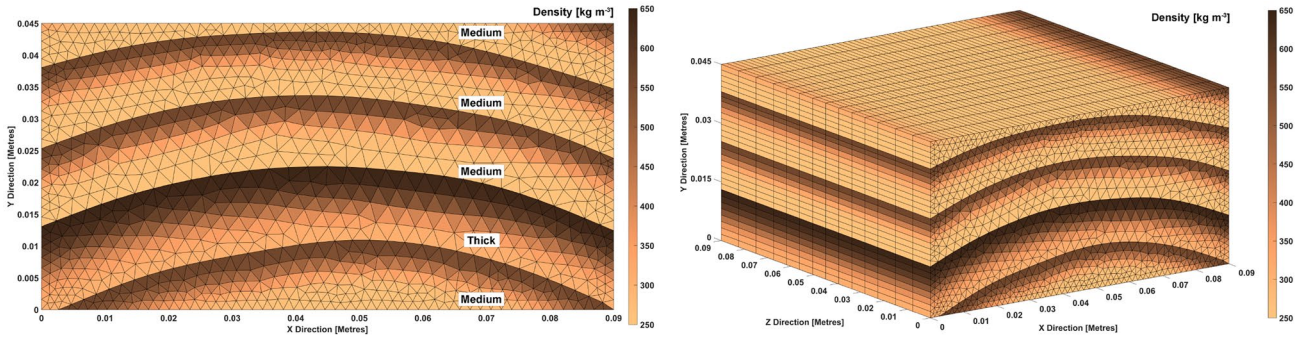

Fig. 18 **a** Two-dimensional mesh populated with density values, where each growth ring is labelled for which 5PL function was used for assigning the density to the elements in that growth ring. **b** Extruded three-dimensional mesh for an example of a typical EWP sample component

where m is the number of elements that surround node i, $\rho_0^{(j)}$ is the density that is associated with element j and A_j is the area of the sub-control volume in element j. Note that as this process is applied to the two-dimensional mesh in the RT plane, our control volumes are considered to be areas. The initial moisture content field is determined by solving a system of nonlinear equations, $\mathbf{f}(\mathbf{s}) = \mathbf{0}$, that enforces the equilibrium of the capillary forces and an overall mass balance throughout the domain (Perré and Turner 2002). The coordinate functions for this system are given as follows:

$$f_i(\mathbf{s}_i) = P_c(S_w^{(i)}, \rho_0^{(i)}, T) - P_c^{\text{eqm}}, \quad i = 1, 2, \ldots, N$$
$$f_{N+1}(\mathbf{s}_i) = \rho_w \frac{\sum_{i=1}^{N} \phi^{(i)} S_w^{(i)} A_i}{\sum_{i=1}^{N} \rho_0^{(i)} A_i} + X_{\text{FSP}} - \overline{X},$$

where N is the number of nodes, $\mathbf{s} = (S_w^{(1)}, S_w^{(2)}, \ldots, S_w^{(N)}, P_c^{\text{eqm}})^T$ is the solution vector containing the free water saturation values at each node and the equilibrium capillary pressure, $\phi^{(i)}$ is the nodal porosity, A_i is the control volume area of node i, and $\overline{X}$ is the averaged moisture content of the timber component. The fibre saturation point, $X_{\text{FSP}} = 0.325–0.001T$, linearly decreases with temperature (Stamm 1961). The nodal moisture content is computed from the free liquid saturation, $S_w^{(i)}$:

$$X^{(i)} = \frac{\phi^{(i)} S_w^{(i)} \rho_w}{\rho_0^{(i)}} + X_{\text{FSP}}, \quad \phi^{(i)} = 1 - \rho_0^{(i)} / \rho_s, \tag{14}$$

where ρ_w is the density of water. The resulting nonlinear system can be solved with an iterative solver such as an inexact Newton's method using first order finite difference approximations for the terms in the Jacobian matrix (Burden et al. 2015). The initial condition for Newton's method is simply that every node has a constant value of $\overline{X}$ and the equilibrium capillary pressure is arbitrarily chosen as 10,000 pascals. The solver typically converges to a solution within 20 iterations with a Newton step size less than 10^{-8}. An example three-dimensional initial moisture content field for a CLT sample with $\overline{X} = 1$ kg (water)/kg (dry solids) for each component is presented in Fig. 19c.

3 Results

The combination of the methodologies described in the previous section allows for the generation of virtual three-dimensional representations of the individual components that form an EWP sample. These virtual representations can be used individually or combined as an EWP sample for numerical simulations involving moisture migration and heat transfer. The mesh contains information on density and pith angle which enable the calculation of the model effective parameters that are defined based on wood density. Fig. 19a–c illustrate an example of a three-layer cross-laminated timber panel section, along with the computed elementwise density, and initial moisture field respectively. We see that the moisture distribution tends to follow the density variation, pooling in the less dense, earlywood regions. From this it is easy to observe the impact of the assumption of negligible longitudinal variation of the material properties on the moisture distribution throughout the CLT panel sample.

To further demonstrate the use of the virtual representation Fig. 20 depicts an example of the use of the two-equation TransPore model to simulate the heat and mass transfer phenomena arising in a prototypical CLT panel section. A summary of the model description, initial and boundary conditions, and numerical solution strategy for this simulation are presented in electronic supplementary material 3. Due to the significant amount of computation time required for simulating three-dimensional moisture migration, we have elected to simulate over a two-layered CLT sample.

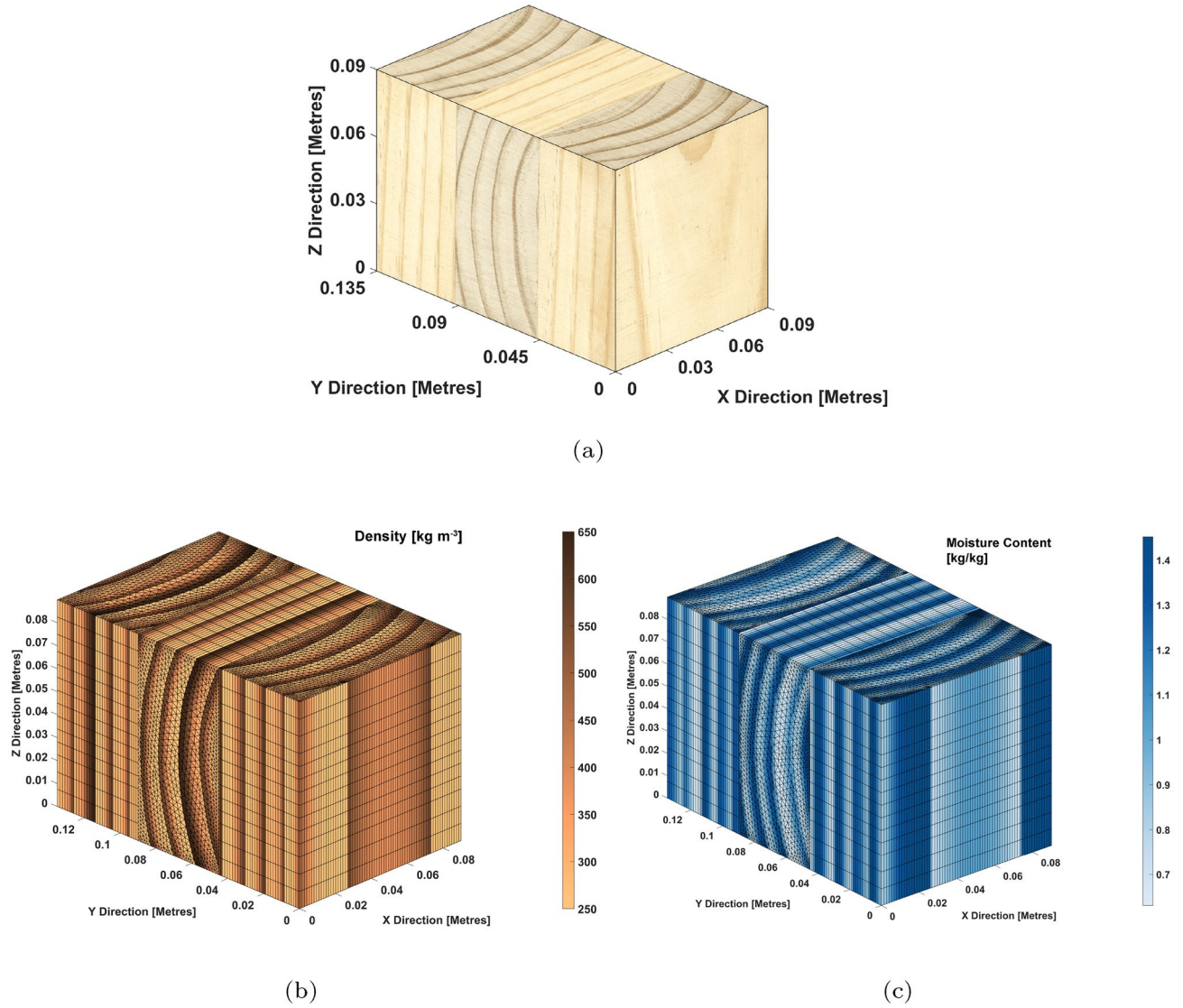

Fig. 19 **a** Texture mapped surface of a 3-layered EWP sample. **b** Elementwise density of the EWP sample. **c** Nodal initial moisture content field with an average initial moisture content of $\bar{X} = 1$ kg (water)/kg (dry solids) for each component

For this simulation, we show the evolution of the moisture, saturation, and temperature fields at 1, 4 and 64 h for the CLT sample subjected to typical climatic conditions experienced in Brisbane, Australia. The leading RT cross-sectional face of the top component is subjected to a saturating boundary condition, while all other faces experience changing psychrometric conditions involving relative humidity and temperature (using fitted cosine functions with a period of 24 h). It can be observed that the moisture field at first migrates along the longitudinal direction of the top component, and slowly approaches near full saturation. Thereafter, the moisture penetrates the second component as it dries and migrates very slowly through the surface due to the influence of the imposed external conditions. In fact, these conditions can lead to a drying phenomenon being evident in the EWP sample. The effects of the growth ring heterogeneity on the moisture and saturation fields are clearly evident in the results. Furthermore, we have modelled the glue line interface between the two components using an imperfect flux boundary condition that allows minimal moisture

Fig. 20 Numerical simulation of heat and mass transfer over 64 h ▶ using the TransPore model in a two-component cross laminated timber panel sample. The first two rows and column display graphs of the averaged moisture content and averaged temperature for each component individually and across the whole product. The plots in the right column graph the wet and dry bulb temperatures and the relative humidity over a 24 h period. Each column of the three-dimensional plots represents moisture content, saturation, and temperature, while each row denotes simulation times at 0, 1, 4, and 64 h respectively

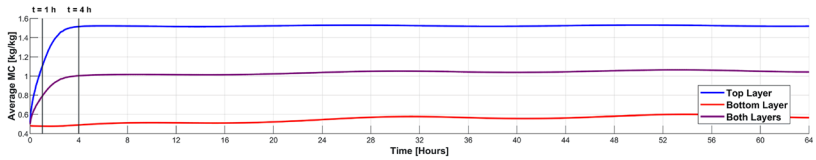
t = 1 h
t = 4 h
Average MC [kg/kg]
Time [Hours]
Top Layer
Bottom Layer
Both Layers

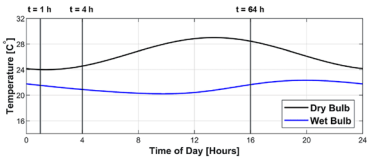
t = 1 h
t = 4 h
t = 64 h
Temperature [C°]
Time of Day [Hours]
Dry Bulb
Wet Bulb

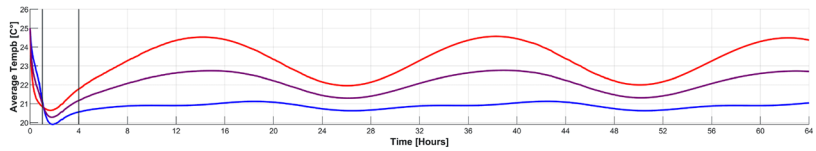
Average Tempb [C°]
Time [Hours]

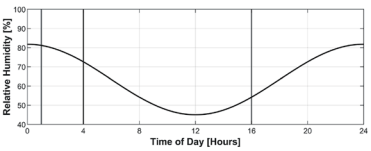
Relative Humidity [%]
Time of Day [Hours]

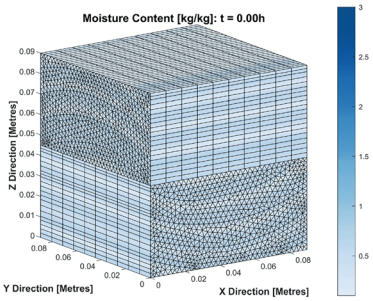
Moisture Content [kg/kg]: t = 0.00h
Z Direction [Metres]
Y Direction [Metres]
X Direction [Metres]

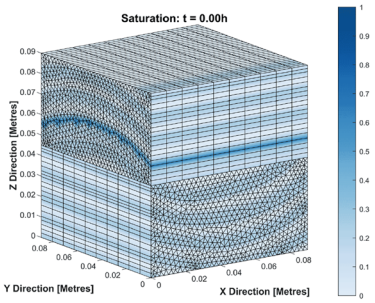
Saturation: t = 0.00h
Z Direction [Metres]
Y Direction [Metres]
X Direction [Metres]

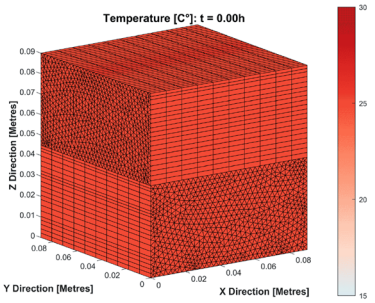
Temperature [C°]: t = 0.00h
Z Direction [Metres]
Y Direction [Metres]
X Direction [Metres]

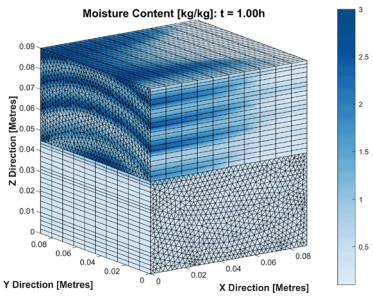
Moisture Content [kg/kg]: t = 1.00h
Z Direction [Metres]
Y Direction [Metres]
X Direction [Metres]

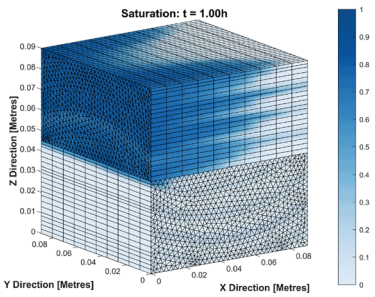
Saturation: t = 1.00h
Z Direction [Metres]
Y Direction [Metres]
X Direction [Metres]

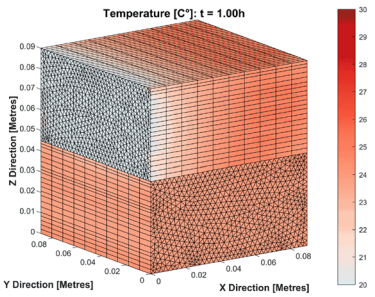
Temperature [C°]: t = 1.00h
Z Direction [Metres]
Y Direction [Metres]
X Direction [Metres]

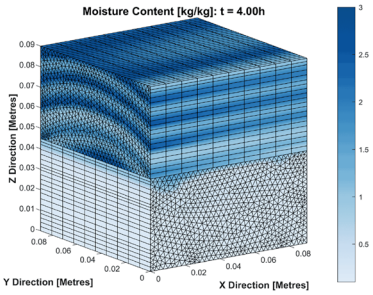
Moisture Content [kg/kg]: t = 4.00h
Z Direction [Metres]
Y Direction [Metres]
X Direction [Metres]

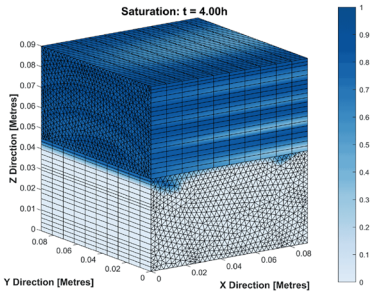
Saturation: t = 4.00h
Z Direction [Metres]
Y Direction [Metres]
X Direction [Metres]

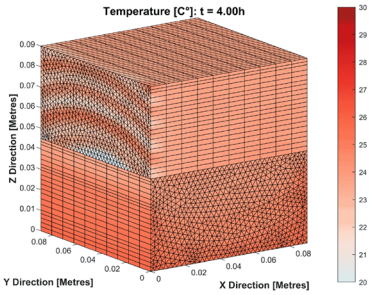
Temperature [C°]: t = 4.00h
Z Direction [Metres]
Y Direction [Metres]
X Direction [Metres]

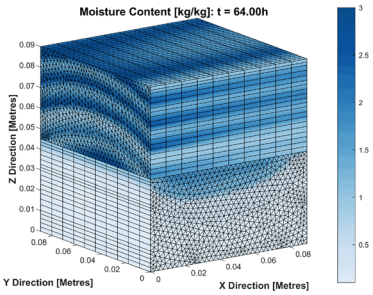
Moisture Content [kg/kg]: t = 64.00h
Z Direction [Metres]
Y Direction [Metres]
X Direction [Metres]

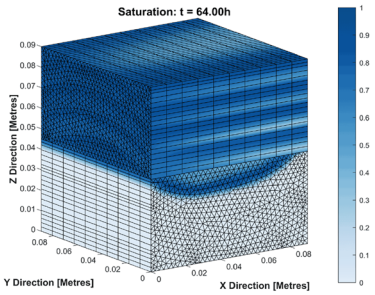
Saturation: t = 64.00h
Z Direction [Metres]
Y Direction [Metres]
X Direction [Metres]

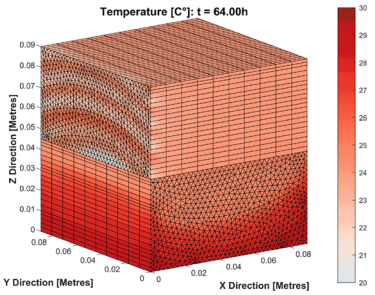
Temperature [C°]: t = 64.00h
Z Direction [Metres]
Y Direction [Metres]
X Direction [Metres]

transfer, while a perfect contact boundary condition is used for the heat flux. Refer to March and Carr (2019) for the definitions of these boundary conditions. The temperature distribution in the EWP sample oscillates according to the variation in the dry and wet bulb temperatures over the 24 h period as expected. This application highlights the capability of the virtual model to facilitate the simulation of moisture ingress and egress through the heterogeneous timber components of the CLT sample. A complete animation of the moisture and temperature variation over the 64 h simulation period is provided in the GitHub repository.

4 Discussion

The aim of this research is to develop a low-cost method for generating virtual representations of engineered wood product samples, accurately capturing the sharp density variations across the growth rings within the mesh geometry. By integrating well-established image analysis techniques, linear algebra, and spectral clustering algorithms, we can achieve three-dimensional reconstructions of these samples. This method offers an alternative to CT scanning, providing users with detailed virtual reconstructions of engineered wood product samples. Our method of virtual reconstruction utilises two important inputs: the first is a grayscale image of the end grain of a timber sample, and the second is a series of anatomical images of the growth ring structure. From the end grain image, we are able to generate a mesh capturing the main macroscopic features (growth ring locations) of the board sample. The growth ring identification also facilitates the identification of the pith location. Next, the anatomical image is used to allow for density variation across the growth ring to enable material properties to be allocated to elements within the mesh. However, it should be noted that the current method, which involves generating a two-dimensional triangular mesh and extruding it into a three-dimensional triangular prismatic mesh, potentially results in the loss of information along the longitudinal direction. This limitation arises from the assumption that the growth ring patterns do not vary longitudinally, which is a reasonable assumption given the small sample sizes we are considering and the constraints of working with a single image where access to the sides of the samples is lost during lamination. Overcoming this challenge and developing a method that incorporates longitudinal variation into the three-dimensional mesh formation process is non-trivial and a topic recommended for future work.

As mentioned above, we have extended the method for locating the pith developed by Habite et al. (2020), where they fitted a series of circles with the same center through the growth rings and a constant averaged growth ring width. This approach may not be suitable for radiata pine due to the varied growth ring width. Our algorithm locates the pith by fitting a possible pith location and growth ring radius for each growth ring individually and then constraining the pith locations to a smaller region until they all converge to the pith. Our algorithm has been tested on three virtual cuts made in the end of a log, depicted in electronic supplementary material 2 (Fig. 2), where we achieved an average absolute error of 11.33 mm from the manually determined pith location. Habite et al. (2020) achieved an average error of 6.99 mm for their samples where the pith was located outside of the board with their largest reported discrepancy being 16.28 mm, which is the largest error that our developed methodology achieved. We believe the iterative pith location algorithm developed in Sect. 2.6 offers a new contribution to the research field and is able to produce plausible pith locations that accounts for irregular growth ring widths and spacings exhibited in wood species such as radiata pine.

We have also demonstrated that the resulting virtual representation is suitable for numerical simulations, in our case moisture ingress. This mesh can be extended to model other physical effects such as stress and strain dynamics, and fungal/rot intrusion. Our results also compare well to the flow patterns observed in work by Burridge et al. (2021), where the denser, latewood regions saturate quickly which is then followed by the earlywood sections. Moreover, flow in the longitudinal direction is significantly faster than the radial and transverse directions which is expected (Perré and Turner 2001a). The example simulation further illustrates the capability of virtual representation for capturing complex moisture flow patterns that would otherwise be impossible to capture in a homogenous modelling framework.

5 Conclusion

This work presents a comprehensive procedure for generating detailed virtual representations of engineered wood product samples. The method utilizes techniques from image analysis and spectral segmentation to generate a two-dimensional unstructured triangular mesh where the elements are aligned along the growth rings. The pith is then located using an interactive constrained least-squares algorithm which has performed consistently to similar methods in the literature. Each element can be assigned a density based on its relative position inside a growth ring using a five-point logistic function fitted from data obtained from three anatomical images. This density variation enables the determination of the initial moisture content field within each component of the EWP sample. Three-dimensional meshes are generated by extruding the two-dimensional triangular meshes

into triangular prismatic meshes, along with the density and moisture information. Lastly, the EWP sample can be reconstructed by combining the meshes of multiple individual timber components. An example simulation was also provided to demonstrate the capability of the virtual representation which exhibited similar flow patterns to those observed in the literature. The main findings of this study were:

- Standard image analysis techniques can be used to generate an image mask highlighting the latewood sections of the growth rings.
- The pith can be well estimated using an iterative constrained least-squares algorithm that fits circles for each growth ring.
- Five-point logistic functions fitted against data obtained from an anatomical images can be used to compute the density across the growth rings.
- The macroscopic features of each wood component can be used to generate a three-dimensional mesh, which can then be combined to form the virtual representation of the entire EWP sample.
- This virtual representation can be used for simulating moisture migration within the EWP sample and captures the impact of the heterogeneous nature of each component on the overall moisture profile.

The method developed in this study has shown great promise in generating a computational mesh that accurately represents the sharp variation in density across the growth rings of EWP samples constructed from radiata pine. The use of image analysis techniques and spectral segmentation is a low-cost approach, making it an attractive alternative to other more expensive and time consuming methods such as X-Ray CT scanning. However, due to the restriction to optical light images of the end grain pattern we have assumed there to be no longitudinal variation in each of the clear wood samples. This assumption is justified by the small sample sizes used in this study so the effect of longitudinal variation is minimal. The virtual representation serves as a foundational platform for future research, allowing for the accurate simulation of heat and mass transfer within these EWP samples. Additionally, by coupling the heat and mass transfer model with stress and strain analysis, it has the potential to unveil the effects of swelling on the structural properties of the EWP samples, providing valuable knowledge for practical applications.

Supplementary Information The online version contains supplementary material available at https://doi.org/10.1007/s00107-024-02132-9.

Acknowledgements The authors would like to acknowledge the Queensland Department of Agriculture and Fisheries, Forest Product Innovation team for supporting the experimental and imaging component of the work. This research was supported by a Queensland University of Technology Postgraduate Research Award which provided Patrick Grant with a stipend during his Doctor of Philosophy candidature. We also thank the reviewers for their insightful feedback that significantly improved the overall presentation of the work.

Author Contributions Patrick Grant: methodology, software, writing - original draft, writing—review and editing, visualisation, project administration, validation, formal analysis, investigation. Steven Psaltis: conceptualisation, methodology, supervision, writing—review and editing, project administration, formal analysis. Maryam Shirmohammadi: conceptualisation, supervision, writing—review and editing, resources, project administration. Ian Turner: conceptualisation, methodology, supervision, writing—review and editing, project administration, formal analysis.

Funding Open Access funding enabled and organized by CAUL and its Member Institutions.

Data availability Code is available on request from the authors or at the github repo: https://github.com/psgrant/TimberMeshGen.

Declaration

Conflict of interest The authors declare that they have no known competing financial interests or personal relationships that could have appeared to influence the work reported in this paper.

References

Abed J, Rayburg S, Rodwell J et al (2022) A review of the performance and benefits of mass timber as an alternative to concrete and steel for improving the sustainability of structures. Sustainability 14(9):5570. https://doi.org/10.3390/su14095570

Burden RL, Faires JD, Burden AM (2015) Numerical analysis. Cengage learning, Boston

Burridge H et al (2021) Identifying efficient transport pathways in early wood timber insights from 3 D X-ray Ct imaging of softwood in the presence of flow. Trans Porous Media 136(3):813–83. https://doi.org/10.1007/s11242-020-01540-8

Carr EJ, Turner IW, Perré P (2011) A new control-volume finite-element scheme for heterogeneous porous media: application to the drying of softwood. Chem Eng Technol 34(7):1143–1150. https://doi.org/10.1002/ceat.201100060

Carr EJ, Turner IW, Perré P (2013) A variable-stepsize jacobian-free exponential integrator for simulating transport in heterogeneous porous media: Application to wood drying. J Comput Phys 233:66–82

Cour T, Benezit F, Shi J (2005) Spectral segmentation with multiscale graph decomposition. In: 2005 IEEE Computer

Society Conference on Computer Vision and Pattern Recognition (CVPR'05), IEEE, pp 1124–113. https://doi.org/10.1109/CVPR.2005.332
De Boor C (1978) A practical guide to splines, vol 27. Springer, New York
Dehariya VK, Shrivastava SK, Jain R (2010) Clustering of image data set using k means and fuzzy K means algorithms. In: 2010 International conference on computational intelligence and communication networks, IEEE, pp 386–39 https://doi.org/10.1109/cicn.2010.80
Downham R, Gavran M (2019) Australian plantation statistics 2019 update. Aust Gov Dep Agric Water Resour Canberra Aust:12
Edelsbrunner H, Mücke EP (1994) Three-dimensional alpha shapes. ACM Trans Graph (TOG) 13(1):43–72. https://doi.org/10.1145/174462.156635
Fang Q, Boas DA (2009) Tetrahedral Mesh Generation From Volumetric Binary and Grayscale Images. In: 2009 IEEE international symposium on biomedical imaging: from nano to macro, Ieee, pp 1142–114 https://doi.org/10.1109/isbi.2009.5193259
Gauch JM (1999) Image segmentation and analysis via multiscale gradient watershed hierarchies. IEEE Trans Image Process 8(1):69–79. https://doi.org/10.1109/83.736688
Geuzaine C, Remacle JF (2009) Gmsh a 3D finite element mesh generator with built in pre and post processing facilities. Int J Numer Methods Eng 79(11):1309–1331. https://doi.org/10.1002/nme.2579
Gevers T, Van De Weijer J, Stokman H (2006). Color Feature Detection. https://doi.org/10.1201/9781420009781.ch9
Habite T, Olsson A, Oscarsson J (2020) Automatic detection of pith location along Norway spruce timber boards on the basis of optical scanning. Eur J Wood Prod 78(6):1061–107. https://doi.org/10.1007/s00107-020-01558-1
Habite T, Abdeljaber O, Olsson A (2022) Determination of pith location along norway spruce timber boards using one dimensional convolutional neural networks trained on virtual timber boards. Construct Build Mater 329:12712. https://doi.org/10.1016/j.conbuildmat.2022.127129
Huber JA, Broman O, Ekevad M et al (2022) A method for generating finite element models of wood boards from X-ray computed tomography scans. Comput Struct 260:106702
Ivković M, Gapare W, Wu H et al (2013) Influence of cambial age and climate on ring width and wood density in pinus radiata families. Ann For Sci 70:525–534
Jia H, Ding S, Xu X et al (2014) The latest research progress on spectral clustering. Neural Comput Appl 24:1477–1486. https://doi.org/10.1007/s00521-013-1439-2
Kong F et al (2021) A deep-learning approach for direct whole-heart mesh reconstruction. Med Image Anal 74:10222. https://doi.org/10.1016/j.media.2021.102222
Koya PR, Goshu AT (2013) Generalized mathematical model for biological growths. Open J Model Simul 201. https://doi.org/10.4236/ojmsi.2013.14008
Lazarescu C et al (2010) Density and moisture profile evolution during timber drying by ct scanning measurements. Dry Technol 28(4):460–467. https://doi.org/10.1080/07373931003613478
Liu L, Jia Z, Yang J et al (2015) A medical image enhancement method using adaptive thresholding in Nsct domain combined unsharp masking. Int J Imaging Syst Technol 25(3):199–205. https://doi.org/10.1002/ima.22137
Liu D, Soran B, Petrie G, et al. (2012) A review of computer vision segmentation algorithms. Lect Notes 53
March NG, Carr EJ (2019) Finite volume schemes for multilayer diffusion. J Comput Appl Math 345:206–223
Mathworks, Inc. (2022) MATLAB function reference R2022a. The Mathworks, Inc., Natick, Massachusetts, p 943. Boundary
Meilă M, Shi J (2001) A random walks view of spectral segmentation. In: International Workshop on Artificial Intelligence and Statistics, PMLR, pp 203–208
Müller AC, Guido S (2016) Introduction to machine learning with Python: a guide for data scientists. O'Reilly Media, Inc
Berti G (2004) Image based unstructured 3d mesh generation for medical applications. In: Neittaanmäki P, Rossi T, Majava K, Pironneau O (editors) European Congress on Computational Methods in Applied Sciences and Engineering (ECCOMAS) 2004
Perré P (1997) Image analysis, homogenization, numerical simulation and experiment as complementary tools to enlighten the relationship between wood anatomy and drying behavior. Dry Technol 15(9):2211–2238. https://doi.org/10.1080/07373939708917359
Perré P (2005) Mesh pore a software able to apply image based meshing techniques to anisotropic and heterogeneous porous media. Dry Technol 23(9–11):1993–2006. https://doi.org/10.1080/07373930500210432
Perré P, Turner IW (1999) A 3-d version of transpore: a comprehensive heat and mass transfer computational model for simulating the drying of porous media. Int J Heat Mass Transfer 42(24):4501–4521
Perré P, Turner I (2001) Determination of the material property variations across the growth ring of softwood for use in a heterogeneous drying model part 1 capillary pressure tracheid model and absolute permeability. Wood Res Technol. https://doi.org/10.1515/hf.2001.052
Perré P, Turner I (2001) Determination of the material property variations across the growth ring of softwood for use in a heterogeneous drying model part 2 use of homogenisation to predict bound liquid diffusivity and thermal conductivity. Wood Res Technol. https://doi.org/10.1515/hf.2001.069
Perré P, Turner I (2002) A heterogeneous wood drying computational model that accounts for material property variation across growth rings. Chem Eng J 86(1–2):117–131. https://doi.org/10.1016/S1385-8947(01)00270-4
Psaltis S, Kumar C, Turner I et al (2021) A new approach for predicting board moe from increment cores. Ann For Sci 78(3):1–1. https://doi.org/10.1007/s13595-021-01093-w
Reinsch CH (1967) Smoothing by spline functions. Numerische Mathematik 10(3):177–183. https://doi.org/10.1007/bf02162161
Shrivakshan G, Chandrasekar C (2012) A comparison of various edge detection techniques used in image processing. Int J Comput Sci Issues (IJCSI) 9(5):269
Siau JF (1984) Transport processes in wood. Springer Series in Wood Science, vol. 2, Springer, Berlin
Stamm AJ (1961) Comparison between measured and theoretical drying diffusion coefficients southern pine. Prod J 11:536–543
The Mathworks, Inc. (2022a) MATLAB. https://au.mathworks.com/products/matlab.html
The Mathworks, Inc. (2022b) MATLAB: Curve Fitting Toolbox. https://au.mathworks.com/products/curvefitting.html?requestedDomain=
Thomas D, Ding G (2018) Comparing the performance of brick and timber in residential buildings—the case of Australia. Energy Build 159:136–147. https://doi.org/10.1016/j.enbuild.2017.10.094
Von Luxburg U (2007) A tutorial on spectral clustering. Stat Comput 17(4):395–416. https://doi.org/10.1007/s11222-007-9033-z
Wood Solutions (2022) 25 King St. [Online; accessed 22/08/2022]. https://www.woodsolutions.com.au/case-studies/25-king-st